Journal of Materials Chemistry A

Sequence-Dependent Self-Assembly of Supramolecular Nanofibers in Periodic Dynamic Block Copolymers

Journal:	*Journal of Materials Chemistry A*
Manuscript ID	TA-ART-11-2023-006695.R1
Article Type:	Paper
Date Submitted by the Author:	27-Nov-2023
Complete List of Authors:	Phong, Jason; Stanford University, Materials Science Engineering Cooper, Christopher; Stanford University, Chemical Engineering Michalek, Lukas; Stanford University, Chemical Engineering Lin, Yangju; Stanford University, Chemical Engineering Nishio, Yuya; Stanford University, Chemical Engineering Shi, Yuran; Stanford University, Chemistry Gong, Huaxin; Stanford University, Chemical Engineering Vigil, Julian; SSRL, Materials Science Division; Stanford University, Chemical Engineering Ilavsky, Jan; Argonne National Laboratory Advanced Photon Source Kuzmenko, Ivan; Argonne National Laboratory, Advanced Light Source Bao, Zhenan; Stanford University, Chemical Engineering

Sequence-Dependent Self-Assembly of Supramolecular Nanofibers in Periodic Dynamic Block Copolymers

Jason K. Phong[1†], Christopher B. Cooper[2*†], Lukas Michalek[2], Yangju Lin[2], Yuya Nishio[2], Yuran Shi[2], Huaxin Gong[2], Julian A. Vigil[2], Jan Ilavsky[3], Ivan Kuzmenko[3], Zhenan Bao[2*].

[1]Department of Materials Science Engineering, Stanford University, Stanford, CA 94305.
[2]Department of Chemical Engineering, Stanford University, Stanford, CA 94305.
[3]Advanced Photon Source, Argonne National Laboratory, Lemont, IL 60439.

[†]Equal Contribution
*Corresponding authors: cbcooper@wustl.edu; zbao@stanford.edu

Abstract

Block copolymers (BCPs) can spontaneously self-assemble into various nanostructured morphologies which enable their diverse applications in selective membranes, polymer electrolytes, and optoelectronics. To expand the range of nanostructures accessible to block copolymers, we designed dynamic block copolymers (DBCPs) that combine the phase separation of traditional block copolymers with the supramolecular self-assembly of periodic dynamic polymers. We demonstrate that DBCPs synthesized with a periodic block sequence self-assemble into high aspect ratio supramolecular nanofibers with well-ordered PEG and PDMS domains, in contrast to those synthesized with a random sequence which do not form nanofibers but have disordered morphologies. The periodicity of the block sequence ensures the regularly spaced placement of the dynamic bonds along the polymer chain, which enables stacking of the hydrogen bonding units into ordered 1D supramolecular nanofibers and delays the onset of terminal flow by up to ~60 °C compared to the random block sequence. The hierarchically assembled supramolecular nanofibers display complex mechanical and thermal phase behavior arising from the interplay between phase separation of the dissimilar polymer backbones and supramolecular interactions between dynamic bonds. Despite identical bulk composition, the periodic DBCPs demonstrate ionic conductivity values over two orders of magnitude higher than their random counterparts due to the formation of well-ordered, interconnected, high aspect ratio ion-transporting PEG domains. These results highlight the potential for DBCPs as an emerging material platform to achieve advanced, self-assembled nanostructured morphologies.

Introduction

The ability for block copolymers (BCPs) to self-assemble into various nanostructured morphologies has received considerable attention in applications including nanolithography,[1,2] nanoporous water filtration membranes,[3] organic optoelectronics,[4] and polymer electrolytes for lithium ion batteries.[5–8] BCPs typically consist of two chemically dissimilar monomer types, which provides a thermodynamic driving force for microscopic phase separation characterized by three factors: the degree of polymerization N, the Flory-Huggins segment-segment interaction parameter χ, and the relative volume fraction f of the components.[9] Due to the covalent linkages between the two polymer backbones, BCP phase separation occurs on the nanometer length scale of the polymer chains, resulting in distinct nanostructured morphologies such as spherical, cylindrical, lamellar, and gyroidal phases.[1] To expand the range or size of nanostructures accessible to block copolymers, strategies including using triblock and star copolymers, discrete block copolymers, or liquid crystalline moieties have been investigated, but are often limited by complex syntheses or processing.[10–14] Moreover, the self-assembly of block copolymers is a result of the frustration due to the competition between the interfacial and chain stretching free energies, which inherently limits the formation of high aspect ratio structures.[15]

An alternative to controlling nanostructure morphology in polymer melts is the incorporation of non-covalent supramolecular interactions (e.g., hydrogen bonds and metal-ligand coordination) also known as interchangeably as dynamic bonds, associative bonds, or stickers.[16,17] For example, previous work has used directional dynamic hydrogen bonding units to achieve robust and complex self-assembled nanostructures with high aspect ratios using a variety of amorphous backbones as well as uniform, segmented polyurethanes and polyureas.[16,18–21] In such systems, hierarchical self-assembly is driven by periodic placement of these dynamic bonds along a homopolymer backbone and depends closely on the geometry of the dynamic bond.[22–24] While supramolecular interactions have been incorporated into block copolymers, most studies focus on telechelic oligomers of dissimilar homopolymers that are end-functionalized with dynamic bonds, which only connect blocks linearly through supramolecular interactions.[25–29] This strategy allows one to readily modulate the effective chain length (N), but does not change the accessible nanostructures compared to traditional BCPs. Other examples include supramolecular diblock copolymers blends that incorporate hydrogen bond donors at the end of one chain and hydrogen bond acceptors at the other end,[29–32] the formation of tubules from diblock oligomers,[33,34] functionalized sugar diblock polymers,[35] and phase-separated vitrimers.[36]

Multiblock copolymers that are covalently linked by hydrogen bonding units which can assemble supramolecularly have been less investigated. In most cases, the hydrogen bonding unit is a dominate part of one block, and not specifically placed at the block junctions, such as hydrogels with hydrogen bonding units embedded in a hydrophobic segment or alternating PEG-peptide chains.[37–39] Here, we design dynamic block copolymers (DBCPs) that combine the phase separation of traditional block copolymers with the supramolecular self-assembly of periodic dynamic polymers to achieve the spontaneous formation of supramolecular nanofibers with well-ordered phase domains. These DBCPs are multiblock copolymers, meaning they consist of multiple oligomers of each block type covalently connected by dynamic hydrogen bonding units at the block junction. We prepared two types of DBCPs in which the oligomer blocks are either (i)

randomly connected or (ii) periodically connected in an alternating sequence (**Figure 1A**). We demonstrate that the DBCPs with a periodic block sequence self-assemble into supramolecular nanofibers with well-ordered domains, in contrast to those with a random sequence which do not form nanofibers but have disordered morphologies (**Figure 1B**). We show that this assembly is driven by the periodicity of the block sequence, which ensures regularly spaced placement of dynamic bonds along the chain backbone and enables stacking of the hydrogen bonding units into ordered 1D supramolecular nanofibers. Compared to random DBCPs of identical composition, periodic DBCPs exhibit delayed onset of terminal flow by up to ~60 °C as well as higher bulk ionic conductivity values by over two orders of magnitude, due to the formation of high aspect ratio nanofibers with well-ordered, interconnected, ion-transporting domains.

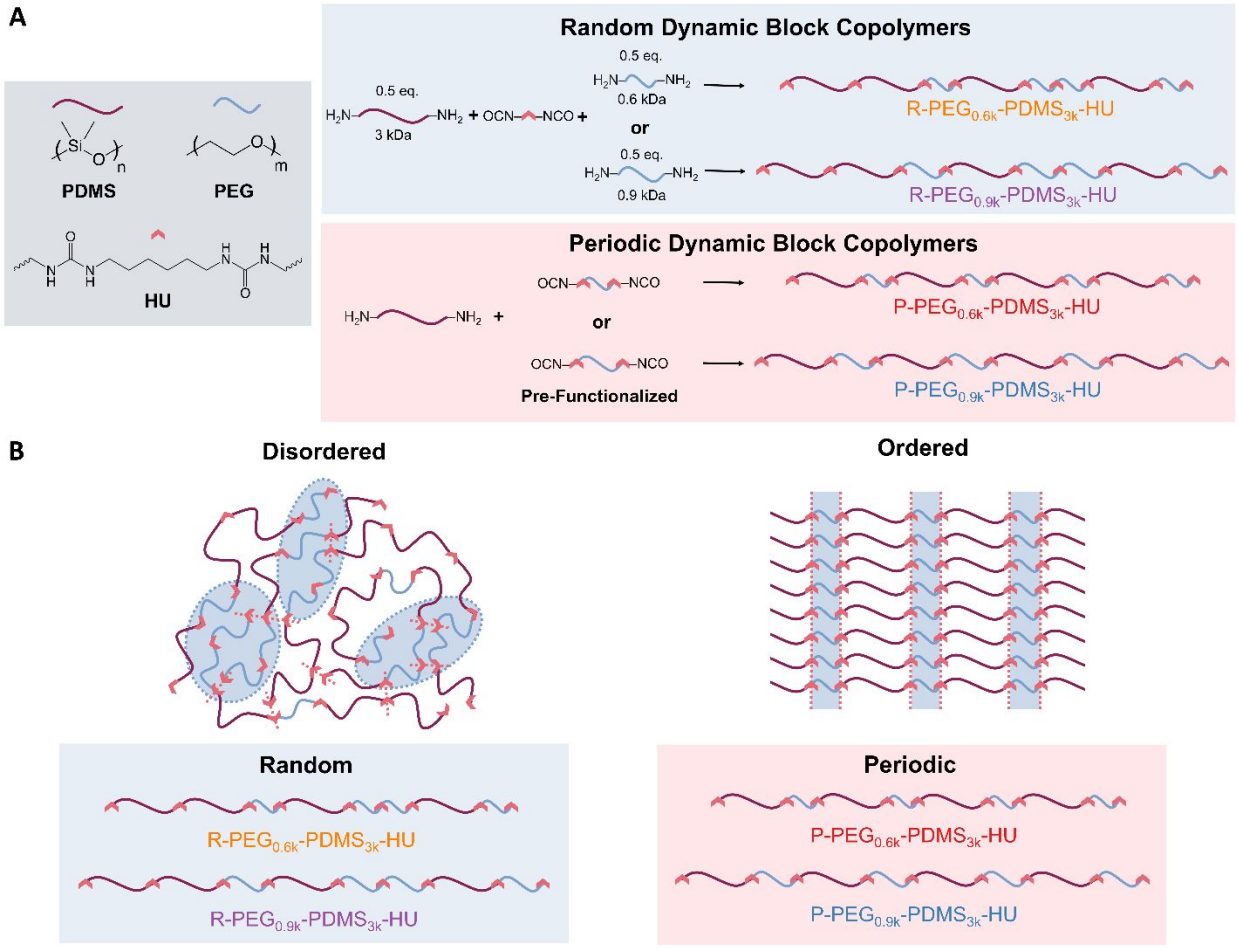

Figure 1. Molecular design and sequence-dependent morphology of random and periodic dynamic block copolymers (DBCPs). (**A**) Random DBCPs are synthesized by simultaneously reacting PEG (0.6 kDa or 0.9 kDa, blue) and PDMS (3 kDa, maroon) oligomers with identical end-group functionalization with HU dynamic bond linkers (red arrows), resulting in a statistically random sequence. Periodic DBCPs are synthesized by pre-functionalizing PEG oligomers with HU units and then reacting with end-functionalized PDMS oligomers to guarantee a strictly alternating periodic sequence. (**B**) The random DBCPs form disordered, amorphous morphologies of the PEG (blue) and PDMS (maroon) domans, while the periodic DBCPs form ordered,

nanostructured morphologies, even for samples with identical chemical composition. The ordered schematic shows alternating PEG (blue) and PDMS (maroon) domains occurring within a self-assembled nanofiber.

Results and Discussion

Molecular Design of PEG-PDMS-HU Dynamic Block Copolymers

We selected polyethylene glycol (PEG) and polydimethylsiloxane (PDMS) as the two oligomer blocks since they both have low glass transition temperatures ($T_{g,PEG}$ = -60 °C, $T_{g,PDMS}$ = -125 °C) and different surface free energies ($\gamma_{PEG} \approx 43$ mJ/m^2, $\gamma_{PDMS} \approx 21$ mJ/m^2).[40,41] This combination enables high segmental motion for the flexible chains to undergo supramolecular self-assembly while having different surface free energies to induce nanoscale phase separation.[26] Depending on the synthetic process used, the two oligomer blocks are covalently linked by the hydrogen-bonding hexamethylene bisurea (HU) units in either a periodic sequence where the PEG and PDMS blocks are strictly alternating (e.g., PEG-PDMS-PEG-PDMS-PEG-PDMS) or in a random sequence where the arrangement of the blocks is statistically determined (e.g., PDMS-PDMS-PEG-PDMS-PEG-PEG) (**Figure 1A, Figure S1**). The synthesized polymers are named first with either *R* (random) or *P* (periodic) to denote the sequence type, the molecular weight of the PEG oligomer (M_n = 0.6 or 0.9 kDa), the molecular weight of the PDMS block (M_n = 3 kDa), and finally the type of dynamic bonding unit, HU (**Table 1**). The PEG oligomer (Jeffamine ED) contains 1-2 monomers of polypropylene glycol at the ends, which limits the crystallinity of the PEG.

We verified the successful synthesis of the polymers by Fourier transform infrared (FTIR) spectroscopy (**Figure S2**), size-exclusion chromatography (SEC, **Table 1**) and ^{1}H nuclear magnetic resonance (NMR) spectroscopy (**Figure S3-5, Table S2**). For DBCPs with the same PEG backbones (i.e., *R-PEG$_{0.6k}$-PDMS$_{3k}$-HU* and *P-PEG$_{0.6k}$-PDMS$_{3k}$-HU*; *R-PEG$_{0.9k}$-PDMS$_{3k}$-HU* and *P-PEG$_{0.9k}$-PDMS$_{3k}$-HU*), changing the block sequence between random and periodic does not affect the FTIR or NMR spectra given that the bulk chemical compositions of the polymers are identical.

Table 1. Dynamic block copolymers with random (R) and periodic (P) block sequences.

Sample Name	PEG:PDMS:HU (wt%)	M_n (kDa)	Đ	Forms Nanofibers in AFM?	SAXS Domain size, *d* (nm)	Young's Modulus, *E* n = 3 (MPa)	Storage Modulus, *G′* at 25 °C (MPa)	G', G" Crossover Temperature on Heating (℃)	Temperature of Last DSC Peak on Heating (℃)	Ionic conductivity, σ at 70 °C n = 2 (S/cm)
R-PEG$_{0.6k}$-PDMS$_{3k}$-HU	15:75:10	13	1.6	No	12	13 ± 2	3.3	66	41	1.1 x 10^{-7}
P-PEG$_{0.6k}$-PDMS$_{3k}$-HU	15:75:10	11	1.5	Yes	9	40 ± 10	6.9	129	133	7.0 x 10^{-6}
R-PEG$_{0.9k}$-PDMS$_{3k}$-HU	21:70:9	17	1.5	No	14	3.3 ± 0.2	2.1	92	78	9.8 x 10^{-8}
P-PEG$_{0.9k}$-PDMS$_{3k}$-HU	21:70:9	16	1.5	Yes	10	12 ± 3	3.7	107	114	2.7 x 10^{-7}

Morphological Characterization

To determine how the block sequence affects the self-assembly of the supramolecular nanofibers, atomic force microscopy (AFM) with quantitative nanomechanical mapping was performed. AFM images showed the formation of supramolecular nanofibers in both periodic DBCPs (*P-PEG$_{0.6k}$-PDMS$_{3k}$-HU* and *P-PEG$_{0.9k}$-PDMS$_{3k}$-HU*) but not in either of the random polymers (*R-PEG$_{0.6k}$-PDMS$_{3k}$-HU* and *R-PEG$_{0.9k}$-PDMS$_{3k}$-HU,* **Figure 2A-D**). Among the synthesized DBCPs, *P-*

PEG$_{0.6k}$-PDMS$_{3k}$-HU exhibits the greatest extent of fiber formation and the highest average indentation modulus observed from the stiffness profiles (15 ± 1 MPa), which is twice that of *R-PEG$_{0.6k}$-PDMS$_{3k}$-HU* (6.6 ± 0.5 MPa), a sample with identical chemical composition that does not form nanofibers (**Figure S6, Table S3**). *P-PEG$_{0.6k}$-PDMS$_{3k}$-HU* also has a higher average indentation modulus than *P-PEG$_{0.9k}$-PDMS$_{3k}$-HU* (11.6 ± 0.8 MPa), which has less fiber formation. We attribute this reduced fiber formation to the diluted influence of hydrogen bonding at larger backbone lengths.

To compare the morphologies of the DBCPs to non-block dynamic polymers with only a single polymer backbone, we also synthesized *PEG$_{0.6k}$-HU* and *PDMS$_{3k}$-HU* polymers (**Figure S7-9**). *PEG$_{0.6k}$-HU* forms the most nanofibers and has the greatest average indentation modulus among the polymers, 70 ± 10 MPa, while *PDMS$_{3k}$-HU* does not form nanofibers and has the lowest average indentation modulus, 5.5 ± 0.2 MPa (**Figure S6**). We hypothesize that the high density of HU units in *PEG$_{0.6k}$-HU* (25 wt%) enables the robust self-assembly of supramolecular nanofibers, while the lower hydrogen bond density of *PDMS$_{3k}$-HU* prevents self-assembly above the entanglement molecular weight of PDMS, consistent with previous reports.[22]

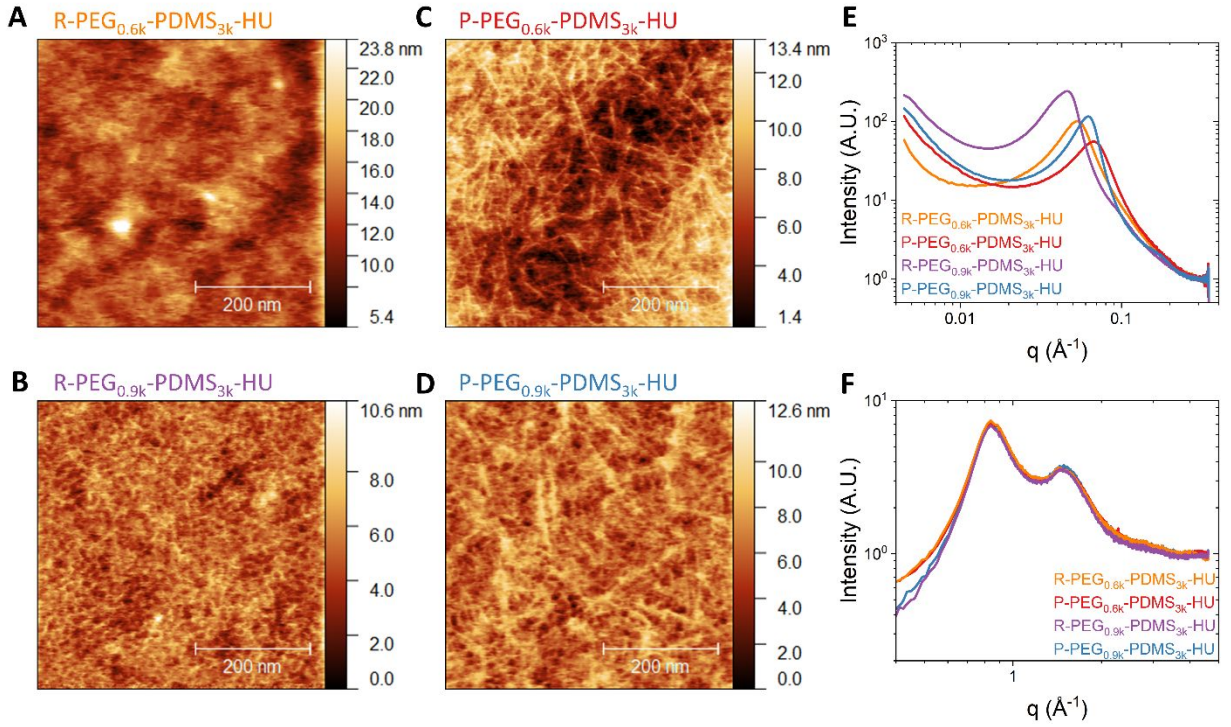

Figure 2. Structural characterization of supramolecular nanofiber formation. AFM height images of (**A**) *R-PEG$_{0.6k}$-PDMS$_{3k}$-HU*, (**B**) *R-PEG$_{0.9k}$-PDMS$_{3k}$-HU*, (**C**) *P-PEG$_{0.6k}$-PDMS$_{3k}$-HU*, and (**D**) *P-PEG$_{0.9k}$-PDMS$_{3k}$-HU* showing that only periodic DBCPs form nanofiber morphologies. Normalized (**E**) SAXS and (**F**) WAXS patterns for *R-PEG$_{0.6k}$-PDMS$_{3k}$-HU* (orange), *P-PEG$_{0.6k}$-PDMS$_{3k}$-HU* (red), *R-PEG$_{0.9k}$-PDMS$_{3k}$-HU* (purple), and *P-PEG$_{0.9k}$-PDMS$_{3k}$-HU* (blue). Periodic DBCPs exhibit smaller SAXS domain sizes than their random counterparts.

The sequence-dependent assembly of the nanofibers suggests that the periodicity of the oligomer blocks and the dynamic bond placement enables the facile formation of ordered 1D nanostructures

from the stacking of directional hydrogen bonds. Moreover, the width of the nanofibers is ~10nm, which is significantly greater than the random coil length of either the PEG or PDMS blocks (~2-4nm), suggesting that the nanofibers include both PEG and PDMS regions with multiple 1D rods of hydrogen bonding units, analogous to the bundled supramolecular fibers reported in PDMS-based periodic dynamic polymers.[22]

To further characterize the differences in morphology, we obtained transmission small-angle X-ray scattering (SAXS) data of the bulk DBCP films which all exhibit a single, broad scattering peak (**Figure 2E**). Comparing the random and periodic DBCPs, we observe that the peaks of the periodic polymers are shifted to higher values of q, the scattering wavevector, than those of the random polymers, which correspond to smaller average domain sizes (d, **Table 1, Table S4**). We attribute the observed peaks (d = 9-14 nm), to the characteristic PEG-PDMS domain spacing in the materials, which is roughly the sum of the random coil lengths of the PEG (~2.3 to 2.8 nm) and PDMS (~3.6 nm) chains, with additional length from the 2 HU linkers which are ~1 nm each (~9 nm total) (**see Note S1**).[42] Moreover, this description is consistent with the larger characteristic *d*-spacings between the PEG and PDMS domains of the random DBCPs arising from the geometric distribution of observing a chain segment of *m* oligomers of the same type in the random polymers. If each chain end has an equal probability of reacting with either a PEG or PDMS oligomer, the probability of observing a chain segment of *m* similar oligomers is:

$$P(m) = \frac{1}{2^m} \quad (1)$$

This yields $< m > \ = 2,$ which suggests that the average chain segment in the random polymers has ~2 PEG or PDMS oligomers in a row. For ideal chains, in which $d \sim N^{1/2}$, the expected ratio between the *d*-spacings of the periodic and random DBCPs is $\frac{d_P}{d_R} = 0.707.$ We calculated these *d*-spacing ratios to be 0.78 for *R-PEG$_{0.6k}$-PDMS$_{3k}$-HU* and *P-PEG$_{0.6k}$-PDMS$_{3k}$-HU* and 0.75 for *R-PEG$_{0.9k}$-PDMS$_{3k}$-HU* and *P-PEG$_{0.9k}$-PDMS$_{3k}$-HU*, consistent with the above analysis. *P-PEG$_{0.9k}$-PDMS$_{3k}$-HU* also has a small peak at 0.17 Å^{-1}, corresponding to a characteristic *d*-spacing of 3.7 nm, which could be attributed to the spacing between the HU units (with a length of ~1 nm) separated by the 0.9 kDa PEG chain (with a random coil length of ~2.8 nm). We note, however, that all of the SAXS patterns lack the sharp peaks traditionally observed in an ordered block copolymer. We attribute this to the dynamic nature of both the PDMS and PEG blocks, which are well above T_g and could obscure the sharp interface required for clear peak resolution.

In the wide-angle X-ray scattering (WAXS) regime, there is no observable difference between the four DBCPs with all scattering patterns containing two peaks at 0.84 and 1.5 Å^{-1}, corresponding to *d*-spacings of 7.5 Å and 4.2 Å (**Figure 2F**). From the scattering patterns of *PEG$_{0.6k}$-HU* and *PDMS$_{3k}$-HU*, we determined that the PEG amorphous halo is the dominant contributor for the peak at 1.5 Å^{-1}, whereas the PDMS amorphous halo is attributed to the peak at 0.84 Å^{-1}, as corroborated by x-ray diffraction (XRD) patterns (**Figure S10-12**). These results suggest that the local environment around the PEG and PDMS backbones is similar between the random and periodic polymers. This is consistent with the identical FTIR spectra, suggesting that the sequence dependance of the bulk properties of the DBCPs arises from morphological differences at larger length scales (> 1 nm). We also do not observe sharp crystalline scattering peaks in this regime in any of the samples, suggesting that the polymers are primarily amorphous. We also do not observe

a clear contribution from the HU units, likely due to their lower number density relative to the two polymer backbones.

Mechanical and Thermal Characterization

Despite their identical bulk compositions, random and periodic DBCPs exhibit dramatically different bulk mechanical properties. Both periodic polymers have a Young's modulus 3-4 times higher than their random counterparts as well as almost double the tensile strength (**Figure 3A, Figure S13, Table S5**). On the other hand, the random polymers are 3-4 times as extensible than the periodic DBCPs. Similar to the AFM data, the high-modulus nanofibers reinforce the bulk periodic DBCP films to withstand greater tensile stress before failure, consistent with previous reports on materials containing hydrogen bonding fibers.[19,22] On the other hand, the random polymers demonstrate higher stretchability, typical of amorphous dynamic polymer networks where dynamic bonds provide a continuous stress-dissipation mechanism.[43]

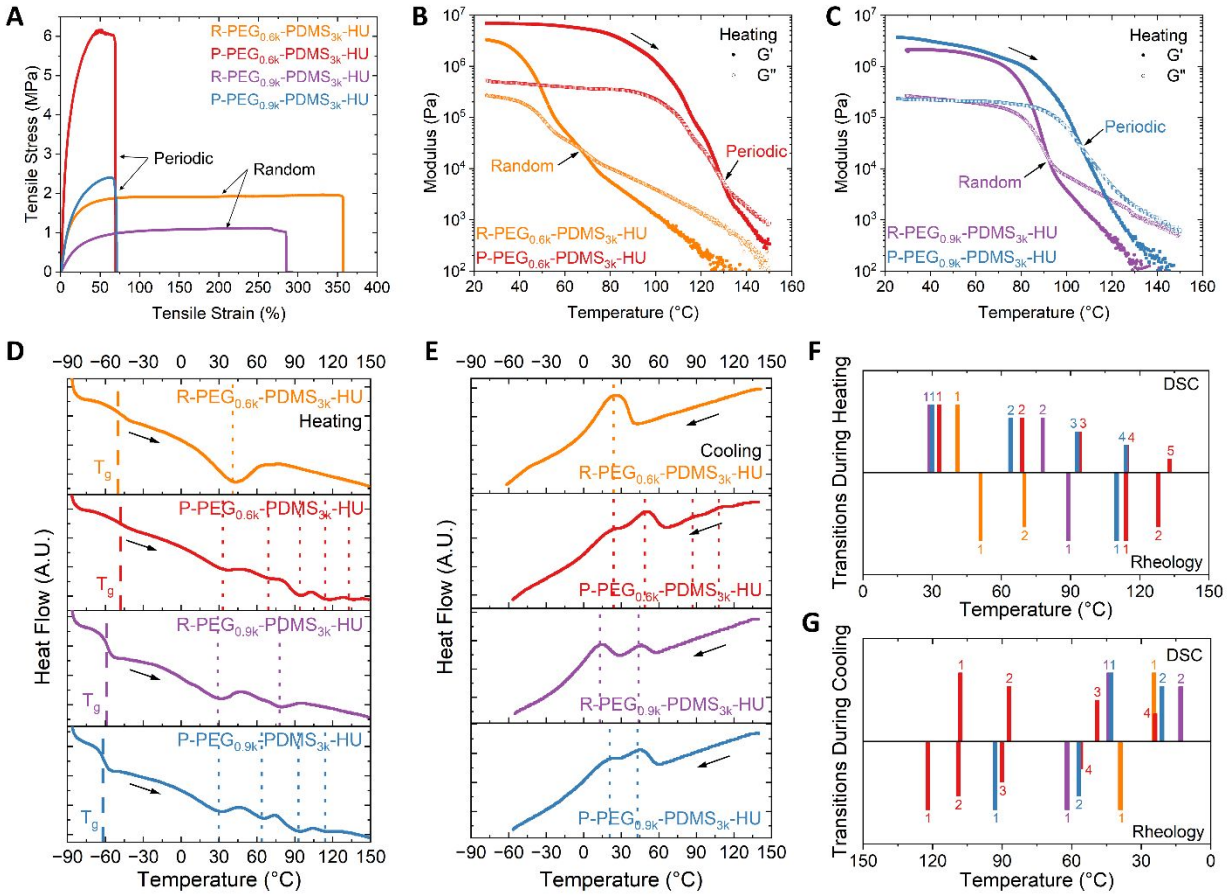

Figure 3. Mechanical and thermal characterization of periodic and random DBCPs. (A) Representative stress-strain curves at room temperature for *R-PEG$_{0.6k}$-PDMS$_{3k}$-HU* (orange), *P-PEG$_{0.6k}$-PDMS$_{3k}$-HU* (red), *R-PEG$_{0.9k}$-PDMS$_{3k}$-HU* (purple), and *P-PEG$_{0.9k}$-PDMS$_{3k}$-HU* (blue) at a strain rate of 200% per minute. Storage (*G',* solid circles) and loss (*G",* open circles) shear moduli during heating for (**B**) *R-PEG$_{0.6k}$-PDMS$_{3k}$-HU* (orange) and *P-PEG$_{0.6k}$-PDMS$_{3k}$-HU* (red), and (**C**) *R-PEG$_{0.9k}$-PDMS$_{3k}$-HU* (purple) and *P-PEG$_{0.9k}$-PDMS$_{3k}$-HU* (blue). Black arrows mark the G', G" crossover point, which is greater for the periodic DBCPs. DSC curves measured during (**D**) heating and (**E**) cooling for *R-PEG$_{0.6k}$-PDMS$_{3k}$-HU* (orange), *P-PEG$_{0.6k}$-PDMS$_{3k}$-HU* (red), *R-*

$PEG_{0.9k}$-$PDMS_{3k}$-HU (purple), and *P-$PEG_{0.9k}$-$PDMS_{3k}$-HU* (blue). Long dashed vertical lines mark the glass transition temperature (T_g) while short dashed vertical lines mark the thermal transitions identified by the derivative of heat flow with temperature. Temperature and number of thermal transitions observed during (**F**) heating and (**G**) cooling via DSC (top) and rheology (bottom).

To further investigate the temperature dependence of the mechanical properties of the DBCPs, we conducted temperature sweep shear rheology between 25 °C and 150 °C. The periodic DBCPs exhibit a crossover between the storage (G') and loss (G") at higher temperatures, by up to ~60 °C, compared to the random DBCPs (**Figure 3B-C, Table 1, Table S6**). For example, the crossover temperature for *P-$PEG_{0.6k}$-$PDMS_{3k}$-HU* is 129 °C during heating and 117 °C during cooling, compared to 66 °C during heating and 54 °C during cooling for *R-$PEG_{0.6k}$-$PDMS_{3k}$-HU,* suggesting that the nanofibers formed by the periodic DBCPs enhance their mechanical thermal stability. Moreover, the shear modulus of the periodic DBCPs is higher than that of the random DBCPs at 25 °C, consistent with the AFM and bulk stress-strain data.

In addition, we noticed multiple plateaus in the shear moduli curves of the periodic DBCPs upon cooling (**Figure S14**). To identify the transition temperatures between these plateaus, we took the derivative $\frac{d(\log G)}{dT}$ of the *G'* and *G"* curves and identified local minima. While the random DBCPs show a single transition during cooling, the periodic DBCPs undergo multiple transitions that occur over a broader temperature range (**Figure S14, Table S7**). During cooling, *P-$PEG_{0.6k}$-$PDMS_{3k}$-HU* exhibits 4 rheological transitions starting from 122 °C to 56 °C, while *P-$PEG_{0.9k}$-$PDMS_{3k}$-HU* exhibits 2 transitions at 93 °C and 57 °C. Since the random DBCPs do not form nanofibers, we hypothesize that they undergo one rheological transition upon cooling from the melt arising from the steady association of the hydrogen bonding units in a relatively amorphous morphology. For the periodic polymers, which do self-assemble into hierarchical nanostructures, we attribute the multiple transitions on cooling to the nucleation and growth of supramolecular nanofibers as HU units stack onto each other to form nanofibers of varying lengths, leading to successively increasing plateau moduli.

To better understand the phase behavior of the DBCPs, we performed differential scanning calorimetry (DSC) between -90 °C and 150 °C (**Figure 3D-E**). DSC shows that the T_g of each pair of random and periodic DBCPs are within 3 °C, suggesting that the local segmental motion associated with the glass transition appears to be independent of the block periodicity and nanofiber morphology (consistent with the FTIR and WAXS data). The heating curves show that the periodic DBCPs undergo more phase transitions than the random polymers do and that these transitions occur at higher temperatures (> 90 °C). Notably, upon cooling, *P-$PEG_{0.6k}$-$PDMS_{3k}$-HU* is the only polymer to exhibit these higher temperature transitions while *P-$PEG_{0.9k}$-$PDMS_{3k}$-HU* undergoes the same number of transitions in the same temperature range as *R-$PEG_{0.9k}$-$PDMS_{3k}$-HU*. The difference between the cooling behaviors of the two periodic DBCPs could be attributed to the more facile formation of supramolecular nanofibers in *P-$PEG_{0.6k}$-$PDMS_{3k}$-HU* as observed through AFM.

Similarly to the rheological experiments, we identified each DSC transition by taking the derivative of the heat flow Q with respect to temperature ($\frac{dQ}{dT}$) , subtracting the heat capacity (C_P)

of the polymer, and determining the transition temperatures by where $\frac{dQ}{dT} - C_P = 0$ (**Figure S15, Table S8**). *P-PEG$_{0.6k}$-PDMS$_{3k}$-HU* undergoes five observable transitions during heating (33 °C, 69 °C, 94 °C, 114 °C, and 133 °C), while *P-PEG$_{0.9k}$-PDMS$_{3k}$-HU* shows four transitions upon heating (30 °C, 64 °C, 93 °C, and 114 °C), which suggests that the supramolecular nanofibers form thermally stable hierarchical structures that successively dissociate or reorder in stages. During cooling, *P-PEG$_{0.6k}$-PDMS$_{3k}$-HU* undergoes four transitions (24 °C, 49 °C, 87 °C, and 108 °C), while *P-PEG$_{0.9k}$-PDMS$_{3k}$-HU* has only two transitions (21 °C and 43 °C) like its random counterpart (13 °C and 44 °C). During both heating and cooling, *R-PEG$_{0.6k}$-PDMS$_{3k}$-HU* exhibits only one peak, while *R-PEG$_{0.9k}$-PDMS$_{3k}$-HU* exhibits two peaks. For both the random and periodic polymers, the last thermal transition observed by DSC is similar to the G', G" crossover temperature observed via rheology (**Table 1**). This provides further evidence that the onset of terminal flow coincides with the final dissociation of stacked HU units. Similarly, upon cooling, both the peaks in the DSC and the G', G" crossover temperature are shifted to lower temperatures. The gap between DSC and rheological transitions on heating and cooling cycles indicates an excess driving force required for dissociation and assembly of the HU units, respectively. Additionally, the total enthalpy changes of the polymers during heating scales with the HU content of the polymers, with ratios of enthalpy change to weight fraction of HU between 0.63 to 0.79, which is consistent with the observation that the thermal transitions are attributed to the association and dissociation of HU units (**Table S9**).

To decouple the effects of nanoscale phase separation in block copolymers and self-assembly in supramolecular polymers, we also used DSC to characterize the thermal behavior of the *PEG$_{0.6k}$-HU* and *PDMS$_{3k}$-HU* polymers as well as a newly synthesized dynamic polymer with a PDMS backbone that uses isophorone bisurea (IU) as the hydrogen bonding unit (*PDMS$_{3k}$-IU*) instead of HU, since the steric hindrance of IU prevents directional hydrogen bonding and thus supramolecular self-assembly (**Figure S8, Figure S16-17**).[44] While *PDMS$_{3k}$-IU* shows no peaks, *PDMS$_{3k}$-HU* exhibits two peaks at 22 °C and 87 °C during heating. The absence of peaks in *PDMS$_{3k}$-IU* further confirms that the observed thermal transitions are due to the aggregation of the HU units. Meanwhile, *PEG$_{0.6k}$-HU*, has one large peak at 57 °C during heating and 10 °C during cooling. As WAXS did not show the characteristic diffraction pattern of crystalline PEG, the observed melting transition is not due to melting of PEG crystals. Instead, we hypothesize that in *PEG$_{0.6k}$-HU*, which lacks the driving force for block copolymer phase separation present in the DBCPs, the stacked HU units assemble and disassemble uniformly in one thermal transition. Thus, we hypothesize that the multiple thermal transitions to assemble and disassemble the supramolecular nanofibers in *P-PEG$_{0.6k}$-PDMS$_{3k}$-HU* and *P-PEG$_{0.9k}$-PDMS$_{3k}$-HU* are a result of the competing driving forces of phase separation between the PEG and PDMS blocks and hydrogen bonding formation between the HU units. That is, at high enough temperatures, we both dissociate the HU units and mix the PEG and PDMS domains due to a decreased χ, and this process can occur in multiple steps over a wide temperature range. We also note that due to the complexity of the transitions, we cannot rule out the formation of 2D aggregates of HU as a secondary interaction to the formation of 1D rods, though we do not observe any morphological evidence of the formation of lamellae-like structures.

Comparing the thermal transitions observed via DSC and rheology together, we observe that only the periodic DBCPs exhibit transitions at temperatures above 90 °C during both heating and

cooling cycles (**Figure 3F-G**). During heating, the DSC peak transition temperatures for the periodic polymers closely align with each other, with all four transitions of *P-PEG$_{0.9k}$-PDMS$_{3k}$-HU* having no more than a 5 °C difference with four of the five transitions of *P-PEG$_{0.6k}$-PDMS$_{3k}$-HU*, suggesting the periodic polymers form nanofibers with a common hierarchical structure that successively dissociates at discrete temperatures (30-33 °C, 64-69 °C, 93-94 °C, and 114 °C, **Table S8**). Likewise, during cooling, the two transitions of *P-PEG$_{0.9k}$-PDMS$_{3k}$-HU* at 43 °C and 21 °C align with two of the four transitions of *P-PEG$_{0.6k}$-PDMS$_{3k}$-HU* at 49 °C and 24 °C. For *P-PEG$_{0.6k}$-PDMS$_{3k}$-HU*, which exhibits the most transitions through both DSC and rheology, the rheological transitions occur at similar temperatures to its DSC peaks (**Table S7-S8**). This provides further evidence that the multi-step association of HU units in *P-PEG$_{0.6k}$-PDMS$_{3k}$-HU* forms supramolecular nanofibers that increase the mechanical properties of the bulk polymer.

In summary, these materials exhibit complex thermal behavior observed by both rheology and DSC. We would like to highlight the following key points:

- Despite identical bulk chemical composition, the periodic DBCPs formed nanofibers and had crossover temperatures of up to 60 °C greater than their random counterparts, indicating that the periodic sequence enables the formation of thermally stable nanofibers that maintains the solid-like properties of the bulk polymers at higher temperatures than the random sequence.
- The periodic polymers exhibited more thermal transitions in both DSC and rheology than the random polymers or the non-block dynamic polymers, due to the complex interplay between phase separation between the PEG and PDMS blocks and hydrogen bonding formation between the HU units.
- The observed transitions can be attributed to the association and dissociation of the HU units, supported by the scaling of total enthalpy change in DSC with HU content, the lack of DSC peaks in PDMS-IU, and the presence of thermal hysteresis in both the DSC and rheology data, which indicates an excess driving force for assembly and disassembly.

Ionic Conductivity

In addition to the differences in the structural, mechanical, and thermal properties of the polymers depending on the block sequence, we examined the effect of block periodicity and the resulting self-assembled nanofibers on bulk ionic conductivity of lithium bis(trifluoromethanesulfonyl)imide (LiTFSI) at various temperatures (**Figure 4A, Table S10**). *PEG$_{0.6k}$-HU* showed higher ionic conductivity than *PDMS$_{3k}$-HU* by two to three orders of magnitude across the temperature range; thus, PEG domains are the preferred ion transport pathways in the DBCPs, consistent with the large body of literature on PEG-based polymer electrolytes.[45,46]

Despite identical chemical composition, the periodic DBCPs have ionic conductivities two orders of magnitude higher than their random counterparts, as expected for materials with different connectivity of PEG microdomains. This enhanced ionic conductivity provides strong evidence that the nanofiber morphology formed in periodic DBCPs contain phase-separated domains of PEG and PDMS (despite the lack of sharp SAXS peaks), which would be necessary to provide the long-range, interconnected, PEG-dense pathways needed for faster ion transport through a bulk polymer comprising mainly PDMS. This is further supported by the fact that the ionic conductivity of *P-PEG$_{0.6k}$-PDMS$_{3k}$-HU*, which forms higher aspect ratio nanofibers via AFM

(**Figure 2**), is at least 5 times greater than that of *P-PEG$_{0.9k}$-PDMS$_{3k}$-HU* despite having lower PEG content. The phase separation of PEG and PDMS domains is additionally reinforced by the observation that at higher temperatures, when the nanofiber morphology begins to successively dissociate (**Figure 3**), the ratio in ionic conductivity between the periodic and random DBCPs decreases (**Figure 4B**).

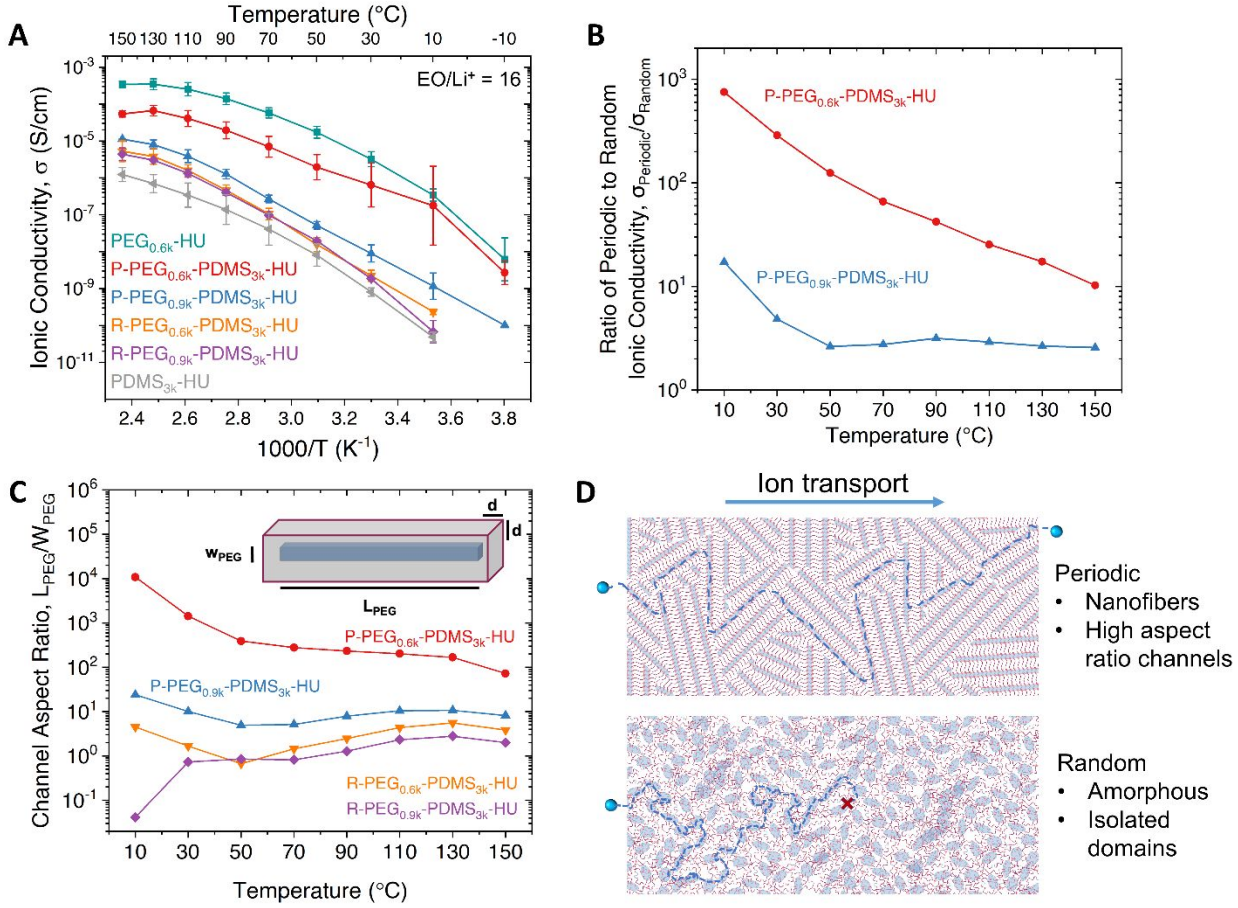

Figure 4. Temperature-dependent ionic conductivity measurements. (**A**) Ionic conductivity values obtained by EIS taken on a temperature sweep from -10 °C to 150 °C for n = 2 samples of *PEG$_{0.6k}$-HU* (teal squares, top), *P-PEG$_{0.6k}$-PDMS$_{3k}$-HU* (red circles), *P-PEG$_{0.9k}$-PDMS$_{3k}$-HU* (blue up-triangles), *R-PEG$_{0.6k}$-PDMS$_{3k}$-HU* (orange down-triangles), *R-PEG$_{0.9k}$-PDMS$_{3k}$-HU* (purple diamonds), and *PDMS$_{3k}$-HU* (gray left-triangles, bottom). (**B**) Ratio of ionic conductivity of periodic to random polymers as a function of temperature, *P-PEG$_{0.6k}$-PDMS$_{3k}$-HU*/*R-PEG$_{0.6k}$-PDMS$_{3k}$-HU* (red circles) and *P-PEG$_{0.9k}$-PDMS$_{3k}$-HU*/*R-PEG$_{0.9k}$-PDMS$_{3k}$-HU* (blue up-triangles). (**C**) Channel aspect ratio calculated from ionic conductivity measurements as a function of temperature for *P-PEG$_{0.6k}$-PDMS$_{3k}$-HU* (red circles), *P-PEG$_{0.9k}$-PDMS$_{3k}$-HU* (blue up-triangles), *R-PEG$_{0.6k}$-PDMS$_{3k}$-HU* (orange down-triangles), and *R-PEG$_{0.9k}$-PDMS$_{3k}$-HU* (purple diamonds). (**D**) Schematic depicting ion transport through periodic (top) and random (bottom) DBCPs. The high aspect ratio channels in the periodic DBCPs enable ion transport to occur primarily in the PEG-phase, while the isolated, low aspect ratio domains of the random DBCPs require ion transport to occur in both the PEG and PDMS domains. A red X denotes the slower transport in the PDMS domains, which limits bulk conductivity.

The observation that *P-PEG$_{0.6k}$-PDMS$_{3k}$-HU* has an ionic conductivity value within an order of magnitude of that of *PEG$_{0.6k}$-HU*, despite having a composition of only 15 wt% PEG, suggests that ion transport occurs almost exclusively through PEG channel-like domains of some average aspect ratio with a small number of hops through short-PDMS domains. To estimate this average PEG channel aspect ratio, we considered that ion diffusion in the bulk DBCPs could be viewed as diffusion through a section of PEG with step size d_{PEG}, followed by a section of PDMS with step size d_{PDMS}, where the total resistance arises from the combination of each individual domain's resistance and step size. Using the ionic conductivities of *PEG$_{0.6k}$-HU* and *PDMS$_{3k}$-HU* as the values for the PEG (σ_{PEG}) and PDMS (σ_{PDMS}) domains, respectively, we determined the effective length ratio of the PEG and PDMS domain step sizes (y) for a given bulk ionic conductivity (σ_{tot}), using the following equation (see **Note S2**):

$$y = \frac{d_{PDMS}}{d_{PEG}} = \frac{\sigma_{tot}^{-1} - \sigma_{PEG}^{-1}}{\sigma_{PDMS}^{-1} - \sigma_{tot}^{-1}} \quad (1)$$

We then estimated the required aspect ratio a needed to achieve this effective length for a PEG channel surrounded by a uniform PDMS shell with a given volume fraction of PEG, ϕ_{PEG} (see **Note S3**):

$$a = \frac{1}{y}\left[\left(\frac{1}{\phi_{PEG}(y+1)}\right)^{1/2} - 1\right] \quad (2)$$

Figure 4C plots this calculated aspect ratio for each DBCP and temperature measured. *P-PEG$_{0.6k}$-PDMS$_{3k}$-HU* has the highest aspect ratios of the DBCPs, over an order of magnitude greater than *P-PEG$_{0.9k}$-PDMS$_{3k}$-HU*, which is consistent with the AFM data showing that *P-PEG$_{0.6k}$-PDMS$_{3k}$-HU* exhibits the greatest extent of fiber formation (**Figure 2**). Moreover, the longest fiber lengths observed in the AFM are ~200 nm. Using the estimated backbone length for the PEG segment (~2.3 nm, **Note S1**) as the channel width, this gives an estimated channel aspect ratio of ~90, which is within an order of magnitude of the aspect ratios calculated using the ionic conductivity data, consistent with the formation of phase-separated PEG and PDMS domains within the nanofiber. Importantly, the qualitative trends in both the AFM and fitted ionic conductivity data are the same, providing strong evidence that the observed differences in ionic conductivity are probing morphological differences between the periodic and random DBCPs (**Figure 4D**). Moreover, as temperature increases, the calculated aspect ratio decreases, consistent with the steady dissociation of the supramolecular nanofibers and the convergence of the ionic conductivities of the random and periodic DBCPs. These results highlight that the self-assembly of the periodic DBCPs into supramolecular nanofibers forms phase-separated pathways for bulk ion transport.

Conclusion

This work highlights the sequence-dependent ability for DBCPs to self-assemble into supramolecular nanofibers. The periodicity of the PEG-PDMS block sequence and the dynamic bond placement enables the hydrogen bonding units of multiple polymer chains to efficiently stack and assemble into well-ordered supramolecular nanofibers. In contrast, the disorder introduced by the random block sequence inhibits the cooperative self-assembly of the dynamic bonds, which

results in dramatically different macroscopic properties despite identical bulk composition. The hierarchical structure of the thermally stable nanofibers give rise to complex rheological and thermal transitions due to the competing effects of phase separation and supramolecular interactions. The robust supramolecular nanofiber formation observed in the periodic DBCPs improves their mechanical properties and as well as their bulk ionic conductivity by creating interconnected PEG-rich pathways for ion transport.

These results demonstrate the potential for enhanced morphological control of block copolymer systems by leveraging multivalent supramolecular interactions. This design concept can be extended to other molecular designs utilizing different polymer backbones (e.g., those with different mechanical properties and surface free energies) and dynamic bonds (e.g., different types of hydrogen bonding units and other non-hydrogen bonding dynamic interactions). The dynamic nature of the supramolecular interactions will also enable the development of new reconfigurable, stimuli-responsive nanostructured materials. The ability to control the self-assembly and ion transport of 1D supramolecular nanofibers could enable future applications such as selective filtration membranes, artificial ion channels, biosensors, controlled drug delivery, and biomimetic materials. We envision that the modular nature of the DBCP synthesis will allow for systematic exploration of the diverse molecular design space to investigate more advanced supramolecular nanostructures beyond nanofiber morphologies.

Experimental Section

Materials

Bis(3-aminopropyl)-terminated poly(dimethylsiloxane) (H_2N-PDMS-NH_2) macromonomers were purchased from Gelest (DMS-A15, M_n = 3 kDa). Diamine-terminated poly(ethylene glycol) (H_2N-PEG-NH_2) macromonomers were obtained from Jeffamine (ED600, M_n = 0.6 kDa and ED900, M_n = 0.9 kDa). Lithium bis(trifluoromethanesulfonyl)imide (LiTFSI) was purchased from TCI America. All other chemicals and solvents were purchased from Sigma-Aldrich. All reagents and oligomers were used as received without further purification.

Synthesis of Random DBCPs (R-$PEG_{0.6k}$-$PDMS_{3k}$-HU and R-$PEG_{0.9k}$-$PDMS_{3k}$-HU)

To synthesize the R-PEG-PDMS-HU polymers, a solution of H_2N-PEG-NH_2 (Jeffamine ED600, M_n = 0.6 kDa and ED900, M_n = 0.9 kDa) and H_2N-PDMS-NH_2 (Gelest DMS-A15, M_n = 3 kDa) in 1:1 molar ratio with ~50 mL anhydrous dichloromethane was prepared under a N_2 atmosphere and placed on ice. Hexamethylene diisocyanate (HDI) was diluted in ~10 mL anhydrous dichloromethane (DCM) and added slowly to the H_2N-PEG-NH_2/H_2N-PDMS-NH_2 solution in a 1:1.03 amine:isocyanate molar ratio. Triethylamine (~1 mL) was added as a catalyst. The resulting mixture was stirred for 24 hours at room temperature. The synthesized polymer was precipitated out of solution by rotary evaporating out approximately half of the dichloromethane to obtain a viscous solution and slowly adding a large excess of acetonitrile. The precipitate was rinsed with acetonitrile three times and subjected to vacuum evaporation for 24 hours at 70 °C. *R-$PEG_{0.6k}$-$PDMS_{3k}$-HU*: ^{1}H NMR ($CDCl_3$, 400 MHz): δ 0.00 (m, 238H), 0.48 (s, 4H), 1.07 (s, 5H), 1.19 (s, 13H), 1.32 (m, 10H), 1.50 (s, 10H), 3.19 (s, 11H), 3.42 (d, 8H), 3.57 (s, 37H). *R-$PEG_{0.9k}$-$PDMS_{3k}$-HU*: ^{1}H NMR ($CDCl_3$, 400 MHz): δ 0.00 (m, 238H), 0.47 (s, 4H), 1.06 (d, 5H), 1.14 (d, 5H), 1.19 (s, 5H), 1.29 (s, 9H), 1.47 (s, 11H), 3.13 (s, 12H), 3.41 (m, 7H), 3.57 (s, 65H).

Synthesis of Periodic DBCPs (P-PEG$_{0.6k}$-PDMS$_{3k}$-HU and P-PEG$_{0.9k}$-PDMS$_{3k}$-HU)
To synthesize the P-PEG-PDMS-HU polymers, a solution of H_2N-PEG-NH_2 (Jeffamine ED600, M_n = 0.6 kDa and ED900, M_n = 0.9 kDa) was prepared in ~20 mL anhydrous DCM. Hexamethylene diisocyanate (HDI) was diluted in ~150 mL anhydrous DCM in a 1:10 amine:isocyanate molar ratio and placed under a N_2 atmosphere and on ice, and then the solution of the PEG oligomers was added slowly. Triethylamine (~1 mL) was added as a catalyst. The resulting mixture was stirred for 24 hours at room temperature. The synthesized OCN-PEG-NCO was precipitated out of solution by rotary evaporating out approximately half of the dichloromethane to obtain a viscous solution. The diisocyanate-terminated PEG oligomers were purified using four liquid-liquid extractions using hexane, which solubilizes the excess HDI, and acetonitrile, which solubilizes OCN-PEG-NCO. OCN-PEG-NCO was isolated by rotary evaporating all the acetonitrile away. OCN-PEG-NCO: ^{1}H NMR ($CDCl_3$, 400 MHz): δ 1.16 (m, 16H), 1.27 (s, 2H), 1.39 (m, 15H), 1.51 (m, 9H), 1.63 (quint, 7H), 2.02 (s, 43H), 3.16 (m, 8H), 3.31 (t, 7H), 3.47 (m, 9H), 3.65 (s, 100H).

A solution of OCN-PEG-NCO in ~50 mL anhydrous DCM was prepared and placed under a N_2 atmosphere and on ice. A solution of H_2N-PDMS-NH_2 (Gelest DMS-A15, M_n = 3 kDa) was prepared in ~15 mL DCM and slowly added to the OCN-PEG-NCO solution. Triethylamine (~1 mL) was added as a catalyst. The resulting mixture was stirred for 24 hours at room temperature. The synthesized polymer was precipitated out of solution by rotary evaporating out approximately half of the dichloromethane to obtain a viscous solution and slowly adding a large excess of acetonitrile. The precipitate was collected using vacuum filtration and rinsed with acetonitrile and subjected to vacuum evaporation for 24 hours at 70 °C. *P-PEG$_{0.6k}$-PDMS$_{3k}$-HU*: ^{1}H NMR ($CDCl_3$, 400 MHz): δ 0.00 (m, 238H), 0.48 (s, 4H), 1.06 (s, 4H), 1.12 (s, 5H), 1.18 (s, 3H), 1.28 (s, 10H), 1.45 (s, 12H), 3.12 (s, 13H), 3.38 (s, 6H), 3.57 (s, 32H). *P-PEG$_{0.9k}$-PDMS$_{3k}$-HU*: ^{1}H NMR ($CDCl_3$, 400 MHz): δ 0.00 (m, 238H), 0.46 (s, 4H), 1.06 (d, 5H), 1.12 (d, 5H), 1.18 (s, 5H), 1.29 (s, 10H), 1.45 (s, 12H), 3.12 (s, 12H), 3.38 (s, 6H), 3.57 (s, 63H).

Synthesis of Non-Block Dynamic Polymers (PEG$_{0.6k}$-HU, PDMS$_{3k}$-HU, PDMS$_{3k}$-IU)
The procedure to synthesize the non-block dynamic polymers was identical to that used to synthesize the R-PEG-PDMS-HU polymers. Briefly, a solution of either H_2N-PEG-NH_2 (Jeffamine ED600, M_n = 0.6 kDa) or H_2N-PDMS-NH_2 (Gelest DMS-A15, M_n = 3 kDa) in ~50 mL anhydrous dichloromethane was prepared under an N_2 atmosphere and placed on ice. Hexamethylene diisocyanate (HDI) or isophorone diisocyanate (IPDI) was diluted in ~10 mL anhydrous dichloromethane (DCM) and added slowly to the solution in a 1:1.03 amine:isocyanate molar ratio. Triethylamine (~1 mL) was added as a catalyst. The resulting mixture was stirred for 24 hours at room temperature. The synthesized polymer was precipitated out of solution by rotary evaporating out approximately half of the dichloromethane to obtain a viscous solution and slowly adding a large excess of acetonitrile. The precipitate was rinsed with acetonitrile three times and subjected to vacuum evaporation for 24 hours at 70 °C. *PDMS$_{3k}$-HU*: ^{1}H NMR ($CDCl_3$, 400 MHz): δ 0.00 (m, 238H), 0.54 (s, 2H), 1.24 (s, 2H), 1.65 (s, 8H), 3.29 (s, 4H). *PEG$_{0.6k}$-HU*: ^{1}H NMR ($CDCl_3$, 400 MHz): δ 0.04 (s, 1H), 1.11 (t, 7H), 1.17 (d, 8H), 1.33 (s, 6H), 1.49 (s, 6H), 3.17 (s, 6H), 3.44 (s, 9H), 3.63 (s, 62H). *PDMS$_{3k}$-IU*: ^{1}H NMR ($CDCl_3$, 400 MHz): δ 0.00 (m, 238H), 0.53 (s, 3H), 0.86 (m, 1H), 0.95 (t, 3H), 1.08 (m, 5H), 1.24 (m, 5H), 1.65 (m, 6H), 3.22 (s, 2H).

Film Preparation
Film samples were prepared by drop-casting ~100 mg/mL solutions in DCM with ~1 mL methanol onto SiO_2 wafers treated with a monolayer of octadecyltrichlorosilane (OTS) to allow for easy film delamination and dried over 12 hours at room temperature and then at 70 °C under vacuum for 24 hours. Film samples were also prepared by heat-pressing at 130 °C for 2 minutes.

NMR Spectroscopy
^{1}H NMR spectra were obtained on a Varian Mercury 400 MHz NMR spectrometer using $CDCl_3$ as the solvent, and the chemical shift was referenced to the residual $CHCl_3$ (7.19 ppm).

FTIR Spectroscopy
ATR-FTIR spectra were recorded using a Nicolet iS50 with a diamond attenuated total reflectance attachment. The thin film samples were placed directly on the sample stage and measured.

Size Exclusion Chromatography
Size exclusion chromatography (SEC) analysis was performed using a Tosoh EcoSEC Ambient (Room Temp)-GPC equipped with two TSK gel GPC columns (G3000Hhr and G4000Hhr; 7.8 mm I.D. × 30 cm, 5 μm) calibrated with a conventional calibration curve using monodisperse polystyrene standards. THF (40 °C) was used as a carrier solvent at the flow rate of 1.0 mL/min. Samples were prepared at 2 mg/mL in THF.

Mechanical Characterization Methods
Room temperature tensile tests were conducted on an Instron 5565 Instrument at a constant strain rate of 200%/min. Rectangular samples with approximate dimensions of 10mm x 4mm x 0.1mm were cut and loaded onto the extensometer with hand- tightened grips using double-sided tape to improve sample-grip adhesion.

Rheological Characterization Methods
Dynamic mechanical analyses were conducted using an Ares G2 Rheometer with an 8 mm parallel plate set-up in a temperature-controlled convection oven. Samples were cut into 8 mm diameter discs with a thickness of ~0.1mm. Temperature sweep tests were collected during heating and cooling between 25 °C and 150 °C at 3 °C/min at 10 rad/s with an applied shear strain of 1% under 0 N axial force. To ensure full contact between the sample and the plates, a pre-conditioning step was used, in which the sample was heated to 150 °C and a frequency sweep was performed from 100 rad/s to 1 rad/s under a compressive force between 0 and 0.05 N.

Differential Scanning Calorimetry
DSC was conducted using a TA instruments Q2000 DSC. Approximately 10 mg of polymer were placed in sealed aluminum pans. Samples were ramped from -90 °C to 150 °C at a rate of 10 °C/min. All samples were heated to 150 °C on an initial heating cycle and cooled to -90°C. Glass transition measurements and peak enthalpies were recorded on the heating and cooling cycle at a ramp rate of 10 °C/minute. Glass transition temperatures and peak enthalpies were extracted using TA Universal Analysis software.

Atomic Force Microscopy Quantitative Nanomechanical (AFM-QNM) Imaging

AFM measurements were collected using a Bruker Icon Dimension instrument with a NSC19/AL-BS AFM probe (from MikroMasch, Tallinn, Estonia nominal with a nominal spring constant of 0.5 N/m, resonance frequency of 60 kHz, and a tip radius of 5 nm). Each AFM probe was initially calibrated against sapphire for exact evaluation of the spring constant and the tip radius was estimated via a TiO_x rough reference sample. Nanomechanical maps were recorded in the Peak Force Quantitative Nanomechanics (PF-QNM) mode while scanning across the cross-sections of the stacked polymer films. All nanomechanical images were recorded at a setpoint of ~1.5 nN with a Peak Force frequency of 2 kHz and amplitude of 150 nm. The scan resolution was set to 256 × 256 pixel with a scan-rate of 0.5 Hz. The data was evaluated and depicted with Gwyddion SPM software. Samples were prepared by spin-coating solutions (60 mg/mL) onto 1 cm × 1 cm silicon wafers at 1000 rpm for 1 minute, annealing at 150 °C for 2 hours, and then slowly cooling to room temperature.

Small-Angle X-ray Scattering (SAXS)

SAXS was conducted in transmission mode on bulk polymer films at beamline 4-2 at Stanford Synchrotron Radiation Lightsource (SSRL) of SLAC National Accelerator Laboratory (SLAC, Menlo Park, CA). Bulk polymer films were tested as free-standing films with a thickness of 0.1mm. The x-ray wavelength was 0.827Å (beam energy 15keV) with a sample-to-detector distance of 3.512m. The Pilatus 1M fast detector was used for 2D scattering data acquisition and reduction into scattering intensity profiles as a function of the scattering vector q was done using customized code at the beamline. For each sample, 10 frames of 1 second exposure were averaged to improve the signal-to-noise ratio. Measurements were performed under ambient conditions. Intensity values were normalized in the high-*q* regime.

Wide-Angle X-ray Scattering (WAXS)

WAXS experiments were conducted at the 20-ID-B beamline at the Advanced Photon Source of Argonne National Laboratory with 21 keV X-ray energy. Data were reduced using Nika and were corrected for the instrumental background as well as appropriate sample container scattering. All measurements were performed under ambient conditions. Intensity values were normalized in the high-*q* regime.

X-ray Diffraction (XRD)

X-ray diffraction patterns were collected on a Bruker D8 Advance powder diffractometer in Bragg-Brentano θ-θ geometry with Cu K_α radiation ($K_{\alpha,1}$:$K_{\alpha,2}$ = 2:1). Solid samples were mounted on an off-cut Si zero-background holder, which spun continuously through the measurement. Where appropriate, these data were converted from 2θ (scattering angle) to *q* (scattering vector, or momentum transfer) using the wavelength of Cu $K_{\alpha,1}$ radiation (λ = 1.54056 Å) owing to the negligible contribution of $K_{\alpha,1}$/$K_{\alpha,2}$ splitting in the angle range of interest.

Ionic Conductivity Measurements

Polymer samples for ionic conductivity measurements were prepared by dissolving the polymers and lithium bis(trifluoromethanesulfonyl)imide (LiTFSI) in a EO:Li^+ molar ratio of 16 in a THF solution (*$PEG_{0.6k}$-HU* was prepared in chloroform as it is insoluble in neat THF). *R-$PEG_{0.6k}$-$PDMS_{3k}$-HU* and *P-$PEG_{0.6k}$-$PDMS_{3k}$-HU* have 4.5 wt% LiTFSI. *R-$PEG_{0.9k}$-$PDMS_{3k}$-HU* and *P-$PEG_{0.9k}$-$PDMS_{3k}$-HU* have 7.8 wt% LiTFSI. *$PEG_{0.6k}$-HU* has 20.8 wt% LiTFSI. *$PDMS_{3k}$-HU*, which has no EO groups, has the same mass loading of LiTFSI as *P-$PEG_{0.6k}$-$PDMS_{3k}$-HU* (4.5

wt%). The solutions were drop-casted onto OTS-treated SiO_2 wafers and dried over 12 hours at room temperature and then at 80 °C under vacuum for 24 hours. The films were heat-pressed at 140 °C into ~100 μm thick films and then cut into approximately 7/32 inch diameter discs which were then heat-pressed between two stainless steel plates inside a 100 μm thick Teflon spacer with an inner diameter of 7/32 inch to control the thickness. Electrochemical impedance spectroscopy (EIS) was measured on a Biologic VSP300 potentiostat station coupled with an ESPEC BTU-133 benchtop temperature chamber at the frequency range of 7 MHz to 100 mHz with an applied bias of 10 mV. Temperature sweep EIS was performed at 20 °C intervals from -10 °C to 150 °C at 20°C/hr. Ionic conductivity was calculated as $\sigma = \frac{l}{R * A}$, where l is the thickness (100 μm), R is the contact resistance obtained at the base of the semicircle in the Nyquist plot, and A is the area of the electrode (0.242 cm^2). The average ionic conductivity of each polymer was calculated from the geometric mean and standard deviation of the values for n = 2 samples upon heating and cooling.

Author Contributions

Conceptualization: C.B.C., J.K.P., and Z.B. Methodology: J.K.P., C.B.C., Y.L., and Y.N. Investigation: J.K.P., C.B.C., L.M., Y.L., Y.N., Y.S., H.G., J.A.V., J.I., and I.K. Visualization: J.K.P., C.B.C., S.E.R., and Z.B. Writing – original draft: J.K.P and C.B.C. Writing – review & editing: J.K.P., C.B.C., L.M., Y.L., Y.N., Y.S., H.G., J.A.V., J.I., I.K., and Z.B. Supervision: Z.B. and C.B.C.

Conflicts of Interest

There are no conflicts of interest to declare.

Acknowledgements

C.B.C. acknowledges support from the Department of Defense (DoD) through the National Defense Science & Engineering Graduate (NDSEG) Fellowship Program. Part of this work was performed at the Stanford Nano Shared Facilities (SNSF), supported by the National Science Foundation under award ECCS-2026822. Use of the Stanford Synchrotron Radiation Lightsource, SLAC National Accelerator Laboratory for SAXS experiments is supported by the U.S. Department of Energy, Office of Science, Office of Basic Energy Sciences under Contract No. DE-AC02-76SF00515. This research used resources of the Advanced Photon Source, a U.S. Department of Energy (DOE) Office of Science user facility operated for the DOE Office of Science by Argonne National Laboratory under Contract No. DE-AC02-06CH11357. The authors thank Prof. Hemamala Karunadasa for support in obtaining the XRD data.{Citation}

References

1 C. J. Hawker and T. P. Russell, *MRS Bull.*, 2005, **30**, 952–966.
2 C. M. Bates, M. J. Maher, D. W. Janes, C. J. Ellison and C. G. Willson, *Macromolecules*, 2014, **47**, 2–12.
3 W. A. Phillip, B. O'Neill, M. Rodwogin, M. A. Hillmyer and E. L. Cussler, *ACS Appl. Mater. Interfaces*, 2010, **2**, 847–853.
4 R. A. Segalman, B. McCulloch, S. Kirmayer and J. J. Urban, *Macromolecules*, 2009, **42**, 9205–9216.

5 E. Glynos, C. Pantazidis and G. Sakellariou, *ACS Omega*, 2020, **5**, 2531–2540.
6 P. M. Ketkar and T. H. Epps, *Acc. Chem. Res.*, 2021, **54**, 4342–4353.
7 M. A. Morris, H. An, J. L. Lutkenhaus and T. H. Epps, *ACS Energy Lett.*, 2017, **2**, 1919–1936.
8 M. W. Schulze, L. D. McIntosh, M. A. Hillmyer and T. P. Lodge, *Nano Lett.*, 2014, **14**, 122–126.
9 F. S. Bates and G. H. Fredrickson, .
10 F. S. Bates, M. A. Hillmyer, T. P. Lodge, C. M. Bates, K. T. Delaney and G. H. Fredrickson, *Science*, 2012, **336**, 434–440.
11 M. Walther and H. Finkelmann, *Progress in Polymer Science*, 1996, **21**, 951–979.
12 L. M. Pitet, E. Alexander-Moonen, E. Peeters, T. S. Druzhinina, S. F. Wuister, N. A. Lynd and E. W. Meijer, *ACS Nano*, 2015, **9**, 9594–9602.
13 Y. Sun, R. Tan, Z. Ma, Z. Gan, G. Li, D. Zhou, Y. Shao, W.-B. Zhang, R. Zhang and X.-H. Dong, *ACS Cent. Sci.*, 2020, **6**, 1386–1393.
14 D. Zhou, M. Xu, Z. Ma, Z. Gan, J. Zheng, R. Tan and X.-H. Dong, *Macromolecules*, 2022, **55**, 7013–7022.
15 A.-C. Shi, *J. Phys.: Condens. Matter*, 2021, **33**, 253001.
16 C. B. Cooper and Z. Bao, *Acc. Mater. Res.*, , DOI:10.1021/accountsmr.2c00101.
17 R. J. Wojtecki, M. A. Meador and S. J. Rowan, *Nature Mater*, 2011, **10**, 14–27.
18 C. B. Cooper, S. Nikzad, H. Yan, Y. Ochiai, J.-C. Lai, Z. Yu, G. Chen, J. Kang and Z. Bao, *ACS Cent. Sci.*, 2021, **7**, 1657–1667.
19 R. M. Versteegen, R. Kleppinger, R. P. Sijbesma and E. W. Meijer, *Macromolecules*, 2006, **39**, 772–783.
20 J. P. Sheth, D. B. Klinedinst, G. L. Wilkes, I. Yilgor and E. Yilgor, *Polymer*, 2005, **46**, 7317–7322.
21 H. N. Ng, A. E. Allegrezza, R. W. Seymour and S. L. Cooper, *Polymer*, 1973, **14**, 255–261.
22 C. B. Cooper, J. Kang, Y. Yin, Z. Yu, H.-C. Wu, S. Nikzad, Y. Ochiai, H. Yan, W. Cai and Z. Bao, *J. Am. Chem. Soc.*, 2020, **142**, 16814–16824.
23 A. Pal, S. Karthikeyan and R. P. Sijbesma, *J. Am. Chem. Soc.*, 2010, **132**, 7842–7843.
24 N. E. Botterhuis, S. Karthikeyan, A. J. H. Spiering and R. P. Sijbesma, *Macromolecules*, 2010, **43**, 745–751.
25 M. C. Stuparu, A. Khan and C. J. Hawker, *Polym. Chem.*, 2012, **3**, 3033.
26 S. K. Yang, A. V. Ambade and M. Weck, *Chem. Soc. Rev.*, 2011, **40**, 129–137.
27 A. Güillen Obando, Y. Chen and Z. Qiang, *Polymer International*, 2022, **71**, 470–477.
28 B. G. G. Lohmeijer and U. S. Schubert, *Angew. Chem. Int. Ed.*, 2002, **41**, 3825–3829.
29 L. M. Pitet, A. H. M. Van Loon, E. J. Kramer, C. J. Hawker and E. W. Meijer, *ACS Macro Lett.*, 2013, **2**, 1006–1010.
30 K. E. Feldman, M. J. Kade, T. F. A. De Greef, E. W. Meijer, E. J. Kramer and C. J. Hawker, *Macromolecules*, 2008, **41**, 4694–4700.
31 C. Tang, S. Hur, B. C. Stahl, K. Sivanandan, M. Dimitriou, E. Pressly, G. H. Fredrickson, E. J. Kramer and C. J. Hawker, *Macromolecules*, 2010, **43**, 2880–2889.
32 D. Montarnal, N. Delbosc, C. Chamignon, M.-A. Virolleaud, Y. Luo, C. J. Hawker, E. Drockenmuller and J. Bernard, *Angew. Chem. Int. Ed.*, 2015, **54**, 11117–11121.
33 Y.-J. He, T.-H. Tu, M.-K. Su, C.-W. Yang, K. V. Kong and Y.-T. Chan, *J. Am. Chem. Soc.*, 2017, **139**, 4218–4224.

34 S. H. Kim, F. Nederberg, R. Jakobs, J. P. K. Tan, K. Fukushima, A. Nelson, E. W. Meijer, Y. Y. Yang and J. L. Hedrick, *Angewandte Chemie*, 2009, **121**, 4578–4582.
35 T. Isono, R. Komaki, C. Lee, N. Kawakami, B. J. Ree, K. Watanabe, K. Yoshida, H. Mamiya, T. Yamamoto, R. Borsali, K. Tajima and T. Satoh, *Commun Chem*, 2020, **3**, 1–9.
36 J. J. Lessard, G. M. Scheutz, S. H. Sung, K. A. Lantz, T. H. Epps and B. S. Sumerlin, *J. Am. Chem. Soc.*, 2020, **142**, 283–289.
37 M. Guo, L. M. Pitet, H. M. Wyss, M. Vos, P. Y. W. Dankers and E. W. Meijer, *J. Am. Chem. Soc.*, 2014, **136**, 6969–6977.
38 G. M. Pawar, M. Koenigs, Z. Fahimi, M. Cox, I. K. Voets, H. M. Wyss and R. P. Sijbesma, *Biomacromolecules*, 2012, **13**, 3966–3976.
39 A. Sarkar, C. Edson, D. Tian, T. D. Fink, K. Cianciotti, R. A. Gross, C. Bae and R. H. Zha, *Biomacromolecules*, 2021, **22**, 95–105.
40 G. Wypych, in *Handbook of Polymers*, Elsevier, 2012, pp. 377–380.
41 G. Wypych, in *Handbook of Polymers*, Elsevier, 2016, pp. 340–344.
42 P.-G. De Gennes, *Scaling concepts in polymer physics*, Cornell University Press, 1979.
43 H. Zhang, Y. Wu, J. Yang, D. Wang, P. Yu, C. T. Lai, A. Shi, J. Wang, S. Cui, J. Xiang, N. Zhao and J. Xu, *Adv. Mater.*, 2019, **31**, 1904029.
44 J. Kang, D. Son, G. N. Wang, Y. Liu, J. Lopez, Y. Kim, J. Y. Oh, T. Katsumata, J. Mun, Y. Lee, L. Jin, J. B. -H. Tok and Z. Bao, *Adv. Mater.*, 2018, **30**, 1706846.
45 P. V. Wright, *Brit. Poly. J.*, 1975, **7**, 319–327.
46 Z. Xue, D. He and X. Xie, *J. Mater. Chem. A*, 2015, **3**, 19218–19253.